



Original Article

Two- and three-dimensional experiments for oxide pool in in-vessel retention of core melts



Su-Hyeon Kim, Hae-Kyun Park, Bum-Jin Chung*

Department of Nuclear Engineering, Kyung Hee University, 1732 Deogyeong-daero, Yongin-si, Gyeonggi-do 17104, Republic of Korea

ARTICLE INFO

Article history:

Received 10 November 2016

Received in revised form

10 May 2017

Accepted 29 May 2017

Available online 26 June 2017

Keywords:

Correlation

In-Vessel Retention

Mass Transfer

Multiplier

Natural Convection

Oxide Pool

ABSTRACT

To investigate the heat loads imposed on a reactor vessel through the natural convection of core melts in severe accidents, mass transfer experiments were performed based on the heat transfer/mass transfer analogy, using two- (2-D) and three-dimensional (3-D) facilities of various heights. The modified Rayleigh numbers ranged from 10^{12} to 10^{15} , with a fixed Prandtl number of 2,014. The measured Nusselt numbers showed a trend similar to those of existing studies, but the absolute values showed discrepancies owing to the high Prandtl number of this system. The measured angle-dependent Nusselt numbers were analyzed for 2-D and 3-D geometries, and a multiplier was developed that enables the extrapolation of 2-D data into 3-D data. The definition of Ra'_H was specified for 2-D geometries, so that results could be extrapolated for 3-D geometries; also, heat transfer correlations were developed.

© 2017 Korean Nuclear Society, Published by Elsevier Korea LLC. This is an open access article under the CC BY-NC-ND license (<http://creativecommons.org/licenses/by-nc-nd/4.0/>).

1. Introduction

In a severe accident, nuclear fuel may melt and stratify into upper metallic and lower mixture (oxide pool) layers according to density differences in the vessel lower head. The mixture layer contains uranium and fission products that continuously generate decay heat. In-vessel retention and external reactor vessel cooling (IVR-ERVC) is a power plant design strategy that allows the operator to maintain the reactor vessel integrity. To implement this strategy, it is important to know the heat load imposed on the reactor vessel by the natural convection of the oxide pool, the heat focusing on the reactor vessel in the upper metallic layer, and the external cooling capacity. This study aims to experimentally determine the heat load imposed on the reactor vessel.

Several experimental studies have been performed in two- (2-D) or three-dimensional (3-D) oxide pool geometries. Numerous volumetric heat sources have been devised to simulate the molten core decay heat. However, results from these studies have been reported without comparison with those of studies, nor have results been verified.

We simulated the IVR phenomena using semicircular (2-D) and hemispherical (3-D) facilities whose heights were 0.042 m, 0.1 m, and 0.167 m; these values correspond to Ra'_H values of 10^{12} – 10^{15} . This work was performed with idealized simplified configurations assuming a homogeneous oxide pool, because complex severe accident phenomena cannot be considered all together.

To achieve these high buoyancies with compact test rigs, mass transfer experiments were performed using a copper sulfate–sulfuric acid (CuSO_4 – H_2SO_4) electroplating system based on the analogous natures of heat and mass transfer (MassTER-OP2 and MassTER-OP3, respectively).

2. Theoretical background

2.1. Phenomena

Typical flow patterns in the oxide pool are shown in Fig. 1 [1]. External cooling induces natural convection flows that run along the curved surface. The main downward flows merge at the bottom, move upward, and then disperse toward the edges at the top plate. There is a secondary natural convective flow beneath the top cooling plate. In a 3-D geometry, the main flows disperse radially beneath the top plate, and gather radially at the center of the bottom. However, these radial behaviors are not expected in a 2-D system.

* Corresponding author.

E-mail address: bjchung@khu.ac.kr (B.-J. Chung).

Nomenclature

A	area (m ²)
C	molar concentration (kmol/m ³)
d	width (m)
D_m	mass diffusivity (m ² /s)
Da	Damköhler number ($q'''H^2/k\Delta T$)
F	Faraday constant (96,485,000 Coulomb/kmol)
g	Gravitational acceleration (9.8 m/s ²)
Gr_H	Grashof number ($g\beta\Delta TH^3/\nu^2$)
h_h	heat transfer coefficient (W/m ² K)
h_m	mass transfer coefficient (m/s)
H	height (m)
I	current density (A/m ²)
I'''	current per volume (A/m ³)
I_{lim}	limiting current density (A/m ²)
k	thermal conductivity (W/m K)
n	number of electrons in charge transfer reaction
Nu	Nusselt number ($h_h H/k$)
Pr	Prandtl number (ν/α)
q	heat generation rate (W)
q'''	volumetric heat generation rate (W/m ³)
R_e	equivalent radius corresponding to pool (m)
Ra_H	Rayleigh number ($GrPr$)
Ra'_H	modified Rayleigh number ($Ra_H Da$)

Sc	Schmidt number (ν/D_m)
Sh	Sherwood number ($h_m H/D_m$)
T	temperature (K)
$t_{Cu^{2+}}$	transference number of Cu ²⁺
U_x	uncertainty of x

Greek symbols

α	thermal diffusivity (m ² /s)
β	volume expansion coefficient (1/K)
γ	dispersion coefficient
δ	boundary layer thickness (m)
μ	viscosity (kg/m s)
ν	kinematic viscosity (m ² /s)
ρ	density (kg/m ³)

Subscripts

b	bulk
dn	lower head
h	heat transfer system
m	mass transfer system
T	thermal
up	top plate
2D	two-dimensional geometry
3D	three-dimensional geometry

2.2. Existing definition of Ra'_H

The buoyancy of a system is expressed by the Rayleigh number. In this system, because the mixture layer of molten fuels continuously emits decay heat, the internal heat generation should be incorporated into the definition of the Rayleigh number. The modified Rayleigh number, Ra'_H , is defined as the product of the conventional Ra_H and the Damköhler number (Da). Da is a dimensionless parameter that represents the volumetric heat generation (q'''), thus:

$$Ra'_H = Ra_H \times Da = \frac{g\beta\Delta TH^3}{\alpha\nu} \times \frac{q'''H^2}{k\Delta T} = \frac{g\beta q'''H^5}{\alpha\nu k}, \quad (1)$$

$$\text{where } Da = \frac{q'''H^2}{k\Delta T}. \quad (2)$$

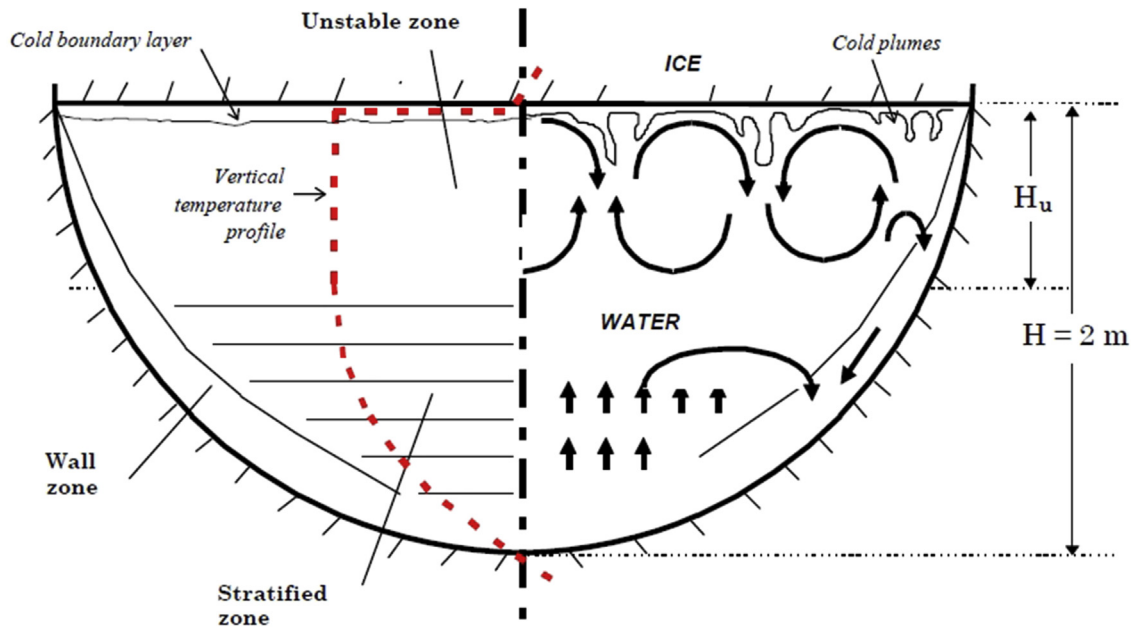


Fig. 1. General flows.

2.3. Previous studies

The experimental studies performed in 2-D and 3-D geometries are summarized in Table 1. Bonnet and Seiler [1] investigated the phenomena using a 2-D semicircular experimental facility (BALI) and developed heat transfer correlations for a curved surface (Nu_{dn}) and top plate (Nu_{up}) between Ra'_H values of 10^{13} and 10^{17} . Lee et al. [2] carried out heat transfer experiments with a 2-D semicircular SIGMA CP facility; correlations of Nu_{dn} and Nu_{up} were determined in the range of 5×10^6 – 7×10^{11} . Kymalainen et al. [3] and Helle et al. [4] carried out heat transfer experiments with 2-D torispherical facilities (COPOL and COPOLII, respectively). Ra'_H was in the range of 10^{14} – 10^{15} for COPOL and 8×10^{14} – 10^{15} for COPOLII; other variables, such as the working fluids, position of the thermocouples, and simulation of the volumetric heat source, were identical. Sehgal et al. [5] investigated natural convection heat transfer phenomena using the 2-D SIMECO facility, which has a semicircular lower section with a vertical cylindrical extension of the upper section. The Ra'_H was 3×10^{13} for water and 1.5×10^{13} for NaNO_3 – KNO_3 . COPOL, COPOLII, and SIMECO do not provide correlations for their experimental results. Asfia and Dhiri [6] performed heat transfer experiments with a 3-D hemispherical facility [University of California, Los Angeles (UCLA), Los Angeles, CA, USA] between Ra'_H values of 5×10^{11} – 8×10^{13} and determined the correlation for the curved surface (Nu_{dn}). Theofanous et al. [7] studied the phenomena with the 3-D hemispherical facility (ACOPO), for Ra'_H values between 8×10^{13} and 2×10^{16} ; correlations for Nu_{dn} and Nu_{up} were developed.

Previous studies [1,3,7] indicate that the local Nu_{dn} increases with the angle of the curved surface, and the maxima were found to be at the uppermost section for BALI, COPOL, COPOLII, and ACOPO. The local Nu_{dn} peaked between 80° and 90° for SIGMA CP and UCLA. In the SIMECO test, the local value decreased between 60° and 70° , and peaked at 80° .

3. Experiments

3.1. Methodology

Heat and mass transfer systems are analogous because the governing equations and parameters are mathematically identical [8]. Table 2 summarizes the dimensionless parameters that govern heat and mass transfer systems [9]. The same mass and heat transfer flows are expected for any given set of Ra'_H , Pr , and Sc values. Therefore, heat transfer experiments can be simulated by mass transfer experiments, and vice versa.

In this study, mass transfer experiments were performed using a CuSO_4 – H_2SO_4 electroplating system to achieve high Ra'_H values with the compact test facilities. When an electrical potential is applied, cupric ions are generated at the anode; they are transferred

Table 2

Corresponding governing parameters of heat and mass transfer systems.

Heat transfer	Mass transfer
$Pr = \frac{\mu}{\alpha}$	$Sc = \frac{\mu}{D_m}$
$Nu = \frac{h_0 H}{k_f}$	$Sh = \frac{h_m H}{D_m}$
$Ra = \frac{g \beta \Delta T H^3}{\alpha \nu}$	$Ra = \frac{g \beta \Delta C H^3}{D_m \nu \rho}$

Nu , Nusselt number; Pr , Prandtl number; Ra , Rayleigh number; Sc , Schmidt number; Sh , Sherwood number.

to the cathode by convection, diffusion, and electric migration. The cupric ions are reduced at the cathode surface, resulting in a decrease in the density of the solution and hence a decrease in the buoyance. The sulfate ions accumulate near the anode, but they do not oxidize and form a layer via equilibrium between electrical migration and mass diffusion. Thus, we can neglect the behavior of the sulfate ions. In this process, the bulk concentration of cupric ions is maintained in a uniform state; this corresponds to the uniform heat generation in heat transfer system.

Levich [10] and Agar [11] proposed the use of an electrochemical system for investigations of heat transfer. Selman and Tobias [12] used this method to derive mass transfer correlations under various conditions. Zaki et al. [13] reported the use of mass transfer experiments. Recently, Chung et al. [14–21] have published experimental mass transfer data to simulate various heat transfer problems. The physical properties were calculated using the relationships in Eqs. (3–10), proposed by Fenech and Tobias [22]. These values are accurate within $\pm 0.5\%$ at 22°C .

$$\rho \left(\text{kg/m}^3 \right) = \left(0.9978 + 0.06406C_{\text{H}_2\text{SO}_4} - 0.00167C_{\text{H}_2\text{SO}_4}^2 + 0.12755C_{\text{CuSO}_4} + 0.01820C_{\text{CuSO}_4}^2 \right), \quad (3)$$

$$\mu(\text{cp}) = 0.974 + 0.1235C_{\text{H}_2\text{SO}_4} + 0.0556C_{\text{H}_2\text{SO}_4}^2 + 0.5344C_{\text{CuSO}_4} + 0.5356C_{\text{CuSO}_4}^2, \quad (4)$$

$$\mu D_m \left(\text{m}^2/\text{s} \right) = (0.7633 + 0.00511C_{\text{H}_2\text{SO}_4} + 0.02044C_{\text{CuSO}_4}) \times 10, \quad (5)$$

$$t_{\text{Cu}^{2+}} = (0.2633 - 0.1020C_{\text{H}_2\text{SO}_4}) \times C_{\text{CuSO}_4}, \quad (6)$$

$$\Delta\rho/\rho = C_{\text{CuSO}_4}(\beta_{\text{CuSO}_4} - \beta_{\text{H}_2\text{SO}_4}(\Delta C_{\text{H}_2\text{SO}_4}/\Delta C_{\text{CuSO}_4})), \quad (7)$$

Table 1

Summary of previous studies.

Facility (dimension)	Pool shape	Working fluid	Ra'	Correlations
BALI (2-D)	Semicircular	Water added cellulose	10^{13} – 10^{17}	$Nu_{up} = 0.383Ra'^{0.233}$ $Nu_{dn} = 0.116Ra'^{0.25}$
SIGMA CP (2-D)	Semicircular	Water and air	5×10^6 – 7×10^{11}	$Nu_{up} = 0.31(Ra'Pr^{-0.36})^{0.245}$ $Nu_{dn} = 0.31(Ra'Pr^{-0.215})^{0.235}$
COPOL (2-D)	Torispherical	ZnSO_4 – H_2O	10^{14} – 10^{15}	—
COPOLII (2-D)	Torispherical	ZnSO_4 – H_2O	8×10^{14} – 10^{15}	—
SIMECO (2-D)	Semicircular under vertical section	Water and NaNO_3 – KNO_3	3×10^{13} , 1.5×10^{13}	—
UCLA (3-D)	Hemispherical	Water	5×10^{11} – 8×10^{13}	$Nu_{dn} = 0.54(Ra')^{0.2}(H/R_e)^{0.25}$
ACOPO (3-D)	Hemispherical	Water	8×10^{13} – 2×10^{16}	$Nu_{up} = 1.95Ra'^{0.18}$ $Nu_{dn} = 0.3Ra'^{0.22}$

2-D, two-dimensional; 3-D, three-dimensional.

$$\Delta C_{\text{H}_2\text{SO}_4} / \Delta C_{\text{CuSO}_4} = -0.000215 + 0.113075\gamma^{1/3} + 0.85576\gamma^{2/3} - 0.50496\gamma, \quad (8)$$

where

$$\gamma = C_{\text{CuSO}_4} / (C_{\text{CuSO}_4} + C_{\text{H}_2\text{SO}_4}), \text{ and} \quad (9)$$

$$\beta_j = 1/\rho [\partial \rho / \partial C_j]_{T, C_{k \neq j}} \quad (10)$$

A limiting current technique was used, because it is difficult to determine the concentration of cupric ions at the cathode surface. When the applied potential increases, the current between the electrodes increases and then reaches a plateau at which the current no longer increases because of exhaustion of all the cupric ions near the cathodes. This is because the reduction of copper ions is faster than the process of transport to the cathode. The constant current is the limiting current, where the concentration of copper ions at the cathode surface is effectively zero, which simulates the isothermal condition in heat transfer system. The mass transfer coefficient h_m can be calculated from the bulk concentration C_b and the limiting current density I_{lim} [23]. The total mass transfer flux is I/nF , and the mass transfer flux component contributed by electric migration is $t_{\text{Cu}^{2+}}I/nF$, which is not represented in a heat transfer system. Therefore, the mass transfer fluxes by diffusion and convection are expressed by $(1 - t_{\text{Cu}^{2+}})I/nF$. When the copper ion concentration is zero at the cathode surface, the mass transfer coefficient becomes:

$$h_m = \frac{(1 - t_{\text{Cu}^{2+}})I}{nF(C_b - C_s)} = \frac{(1 - t_{\text{Cu}^{2+}})I_{\text{lim}}}{nFC_b}. \quad (11)$$

Using the analogy between heat and mass transfer, the Damköhler number for mass transfer is:

$$Da_m = \frac{(1 - t_n)I''H^2}{nFD_m\Delta C}, \quad (12)$$

where the electrical current density (I''), copper sulfate concentration difference (ΔC), and mass diffusivity (D_m) are equivalent to the volumetric heat generation rate (q'''), temperature difference (ΔT), and thermal conductivity (k), respectively [19].

In a mass transfer system, Ra'_H is defined as:

$$Ra'_H = \left(\frac{gH^3\Delta\rho}{D_m\nu\rho} \times \frac{128.5\Delta C}{\Delta\rho} \right) \left(\frac{(1 - t_n)I''H^2}{nFD_m\Delta C} \right) = 0.1285 \frac{(1 - t_n)gI''H^5}{nD_m^2\nu\rho F}. \quad (13)$$

By adopting mass transfer methods, we are able to efficiently simulate the prime characteristics of the mixture layer: high Ra' with small facility, uniform heat generation, and isothermal cooling condition.

3.2. Experimental facility

The MassTER-OP2 and MassTER-OP3, with heights 0.042 m, 0.1 m, and 0.167 m are shown in Figs. 2A–2F. For the MassTER-OP2, the widths were 0.0168 m, 0.04 m, and 0.0668 m, to give a thickness/height ratio (d/H) of 0.4, which is greater than the value of 0.25 recommended by Dinh et al. [24]; as such it is possible to neglect sidewall effects. Figs. 2G and 2H indicate the volumetric heat sources for MassTER-OP2 and MassTER-OP3, respectively.

Copper cathode electrodes were placed on the inner surfaces. A one-piece electrode was positioned in one half of the chamber, and

a total of 13 electrodes were aligned in the other half; nine were positioned on the curved surface ($0-90^\circ$), and four were placed on the top plate to measure the local values. The current measured by the one-piece electrode was compared with the sum of the individual electrode current, so that the effects of the insulation layers between the electrodes could be identified. To simulate the volumetric heat source, the copper anodes were attached to both side walls of the MassTER-OP2 and, based on the results of comparative tests of volumetric heat sources, a copper cruciform electrode was connected to the center of the MassTER-OP3 top plate [25,26]. Fig. 3 shows the experimental circuit.

The cathode simulates a hot wall in the heat transfer system, because the reduction of cupric ions near the cathode surface decreases the fluid density, causing buoyancy. Konishi et al. [27] highlighted the need for reliable cathode measurements. Therefore, we performed the tests with the apparatus inverted in the direction of gravity, as shown in Fig. 3, resulting in natural convection flows toward the center of the curved surface.

3.3. Test matrix

Table 3 summarizes the test matrix. The experiments were performed using semicircular and hemispherical facilities of three different sizes, resulting in six Ra'_H values. Sc was 2,014, which corresponds to Pr in a heat transfer system.

3.4. Uncertainty analysis

We used a data reduction technique to analyze the uncertainty of the mass transfer experiments [28]. As the Sherwood number is the final dependent variable, the uncertainty can be expressed as follows:

$$Sh_H = \frac{h_m H}{D_m} \Rightarrow Sh_H = f(h_m, D_m, H) \text{ and} \\ U_{Sh_H}^2 = \left(\frac{\partial Sh_H}{\partial h_m} U_{h_m} \right)^2 + \left(\frac{\partial Sh_H}{\partial D_m} U_{D_m} \right)^2 + \left(\frac{\partial Sh_H}{\partial H} U_H \right)^2 \quad (14)$$

The uncertainties of h_m and D_m were further estimated in the same way as in Eq. (14), until only basic measurement quantities, such as the length, electric current, and masses of H_2SO_4 and CuSO_4 , remained. We assumed that the measurement errors of these quantities were half of the smallest measurable interval. The errors in length, mass, and current measurement were estimated to be 2.5×10^{-5} m, 5×10^{-7} kg, and 5×10^{-5} A, respectively. The fractional uncertainty was 1.3%, which indicates the good accuracy of the experimental technique.

4. Results and discussion

4.1. Reliability of the piecewise electrodes

Table 4 shows the relative errors of the current measured by the one-piece electrode and the sum of the currents measured by the nine individual electrodes for MassTER-OP2 and MassTER-OP3, respectively. The differences are within 12% on the curved surface and 16% at the top plate. This indicates that the effects of the insulation layers between the piecewise electrodes are negligible.

4.2. Specification of Ra'_H definition

There is no standard definition for volumetric heat generation (q'''), which is an important component of Ra'_H . q''' could be defined as the total heat divided by the cube of the height (q/H^3), or by the

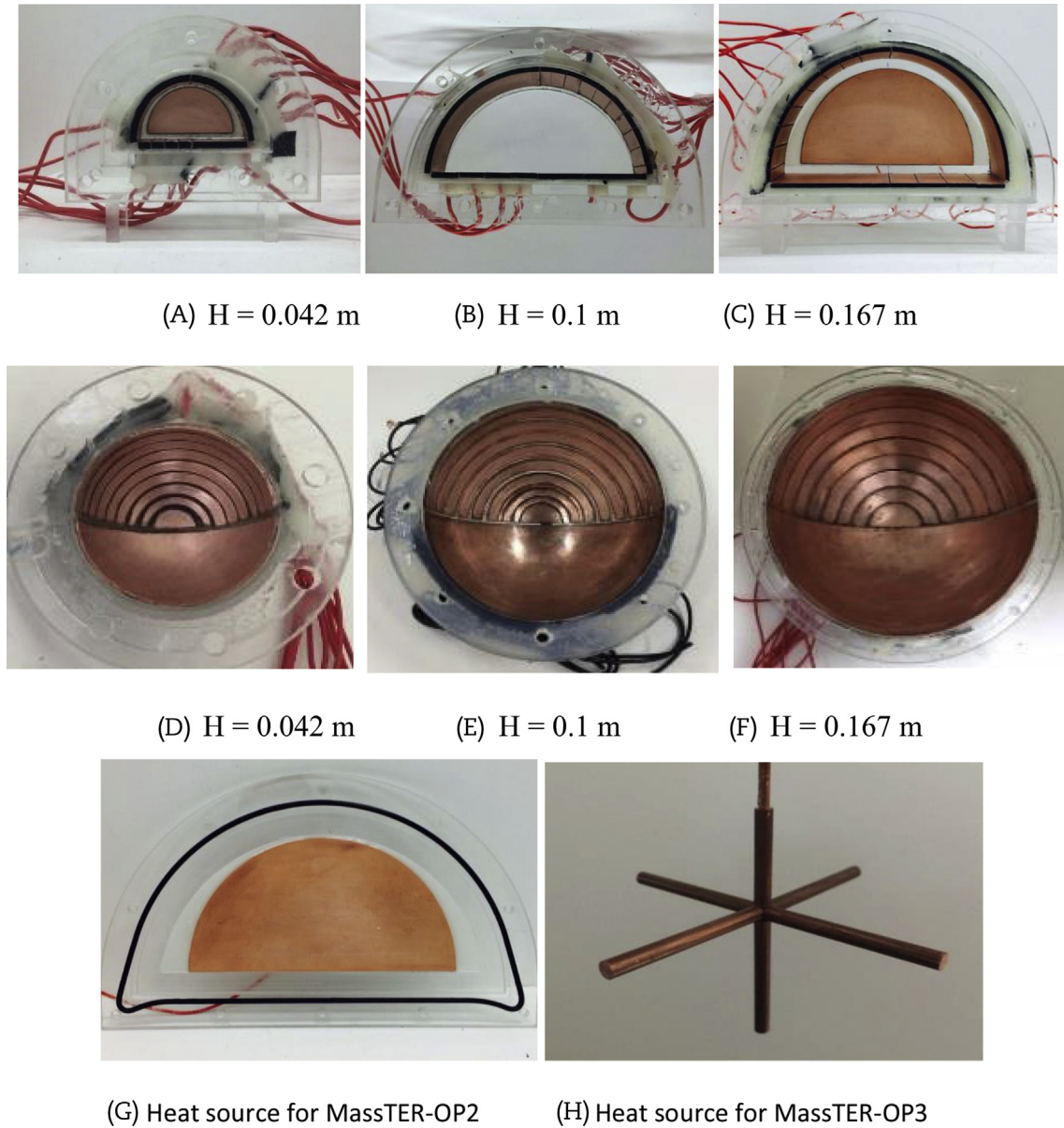


Fig. 2. Experimental facilities. (A) $H = 0.042$ m. (B) $H = 0.1$ m. (C) $H = 0.167$ m. (D) $H = 0.042$ m. (E) $H = 0.1$ m. (F) $H = 0.167$ m. (G) Heat source for MassTER-OP2. (H) Heat source for MassTER-OP3.

volume (q/V). Both definitions could be used for the 3-D facility because the characteristic length is only H . However, q/H^3 is clearly inappropriate for the 2-D facility as it ignores the width. Therefore, the proper definition of q''' for 2-D and 3-D geometries is q/V , which allows 2-D and 3-D experimental results to be compared.

4.3. Comparison of measured mean Nu with values from existing studies

The mean Nu of the MassTER-OP, and values from existing studies of the curved surface and top plate, are compared in Fig. 4. The black lines indicate existing correlations, with dashed lines for 2-D and solid lines for 3-D. Circles and squares indicate the results of MassTER-OP2 and MassTER-OP3, respectively. It is clear that the existing 2-D and 3-D results have only a weak correlation. Here, the MassTER-OP2 and MassTER-OP3 results were found to correlate strongly. We suggest that this is because the MassTER-OP

experiments were performed with identical heating methods, working fluids, and methodology: the only difference was the geometry. Previous studies have varied the methodology. Also, the results correlated more strongly because a proper definition of the volumetric heat source ($q''' = q/V$) was used. Correlations for the measured Nu 's were developed for the curved surface (Nu_{dn}) and top plate (Nu_{up}), as follows:

$$Nu_{up} = 1.046Ra_H'^{0.211} \quad \text{and} \quad (15)$$

$$Nu_{dn} = 0.27Ra_H'^{0.209} \quad (16)$$

These are represented by red lines in Figs. 4A and 4B.

The measured mean Nu_{dn} values were 37% less than those values in the BALI and ACOPO data, whereas the measured mean Nu_{up} values were 35% greater than the BALI correlation and 47% greater than the ACOPO correlation. This is attributable to the high

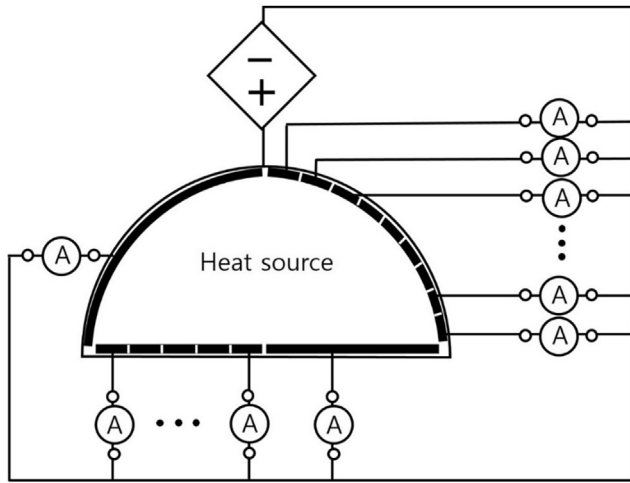


Fig. 3. Experimental circuit.

Table 3
Test matrix.

Facility		Ra'	Pr
MassTER-OP2	$H = 0.042$ m	4.55×10^{12}	2,014
	$H = 0.1$ m	1.11×10^{14}	
	$H = 0.167$ m	8.99×10^{14}	
MassTER-OP3	$H = 0.042$ m	8.64×10^{12}	
	$H = 0.1$ m	2.02×10^{14}	
	$H = 0.167$ m	1.46×10^{15}	

Pr value used in this study. When Pr was greater than 1, as shown in Fig. 5, the velocity boundary layer was thicker than the thermal boundary layer ($\delta_T < \delta$). This means that the plume rising from the bottom contains less cooled fluid, which enhances the heat transfer in the top plate. Therefore, the mean Nu_{up} s measured in MassTER-OP, where the Pr was 2,014, were greater than those of existing studies with Pr values less than 10. However, the total mean Nu , the summation of Nu_{dn} and Nu_{up} , was 10% greater than that value in the BALI data, and 16% greater than that in the ACOPO data. In conclusion, when mass transfer with high Pr was used to simulate heat transfer, the heat flux ratio between the curved surface and the top plate differed because of the difference in Pr , but the total heat flux was similar. Thus, Eqs. (15) and (16) should incorporate the influence of Pr prior to IVR application and further accumulation of the experimental database.

4.4. Comparison of local Nu between MassTER-OP2 and MassTER-OP3

4.4.1. Curved surface

The local Nu_{dn} values along the MassTER-OP2 and MassTER-OP3 curved surfaces for various Ra'_H values are shown in Fig. 6. The Nu_{dn}

Table 4
Relative errors in the measured currents between one-piece and piecewise electrodes.

	MassTER-OP2			MassTER-OP2		
H (m)	0.042	0.1	0.167	0.042	0.1	0.167
Curved surface (%)	-11.53	0.31	1.86	-4.24	-7.64	2.26
Top plate (%)	11.98	-14.44	9.43	15.60	-2.73	0.41

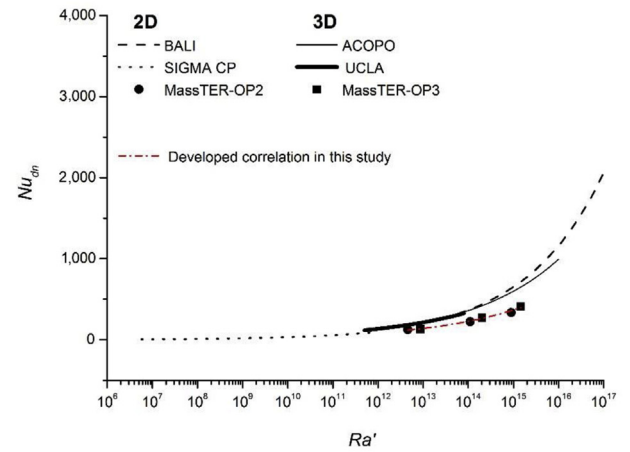
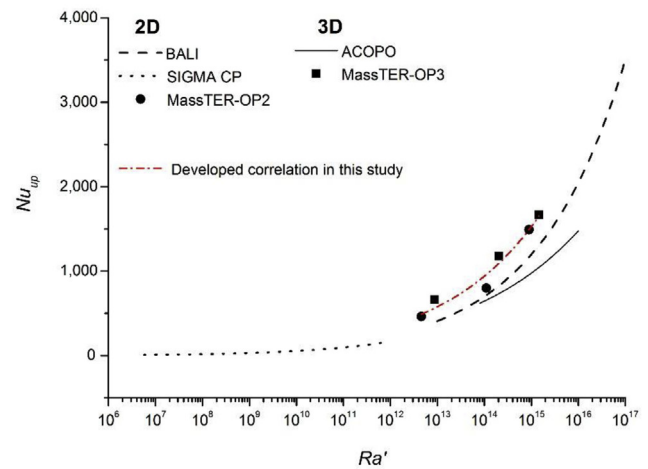
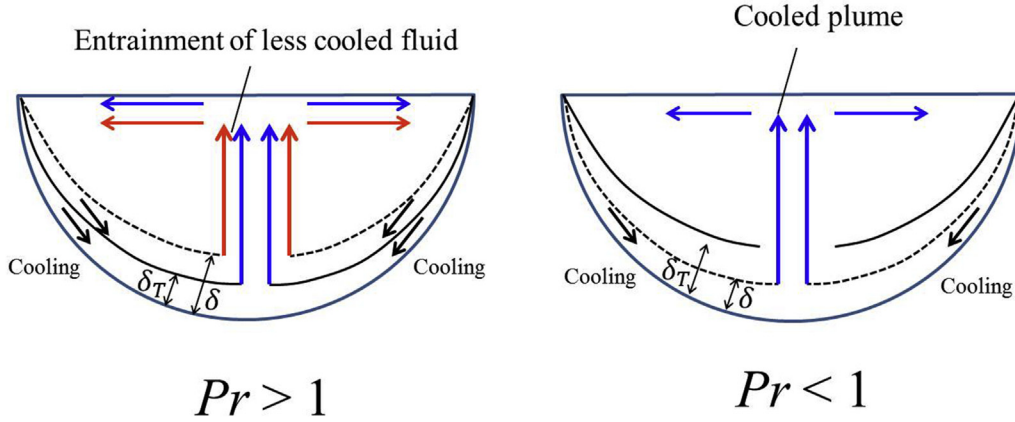
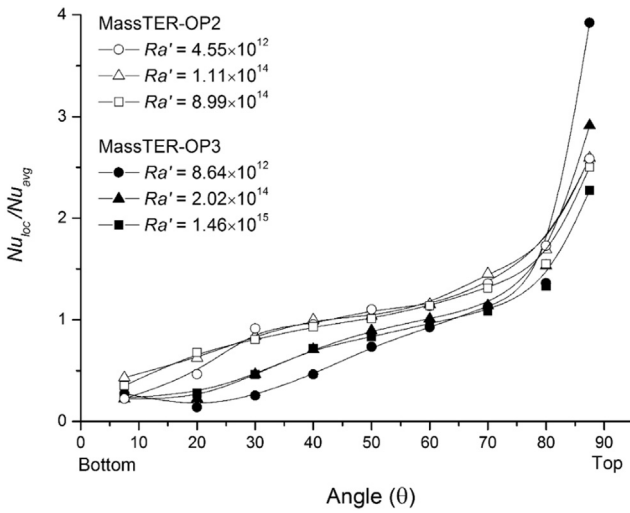
(A) Mean Nu_{dn} of the curved surface(B) Mean Nu_{up} of the top plate

Fig. 4. Comparison of mean Nu with existing correlations for the curved surface and top plate. (A) Mean Nu_{dn} of the curved surface. (B) Mean Nu_{up} of the top plate.

ratios increase with the angle of the curved surface in all cases regardless of Ra'_H . However, the 2-D and 3-D results differed slightly because of the differences in flow, as shown in Fig. 7. The natural convective flows run down the curved surface, combine at the bottom, and move upward; the rising flows disperse underneath the top plate to the edges. In a 2-D geometry, these flows move on a plane, whereas the downward flows merge at a point, and the upward flows disperse radially in a 3-D geometry. These differences result in the variation of local Nu_{dn} .

In the 80–90° section, the Nu_{dn} ratios for MassTER-OP2 were independent of Ra'_H , whereas the ratios from MassTER-OP3 were dependent on Ra'_H . This is because, in a 2-D geometry, the dispersed flows underneath the top plate are inversely proportional to H (linear scattering); flows are inversely proportional to H^2 (radial scattering) in a 3-D geometry. Therefore, the dispersed flows are reduced more significantly in the 3-D system. These dispersed flows influence the initial velocity of the natural convective flows of the curved surface, resulting in a difference between the 2-D and 3-D results in the 80–90° section.

The results of MassTER-OP2 were greater than those of MassTER-OP3 at the lower section of the curved surface. As shown in Fig. 7, the downward flows run toward a point in the curved surface for the 3-D geometry, but not for the 2-D geometry.

Fig. 5. Difference of flow depending on Pr . Pr , Prandtl number.Fig. 6. Comparison of angle-dependent Nu_{dn} for the curved surface between MassTER-OP2 and MassTER-OP3.

Therefore, in the 2-D facility, the thickness of the boundary layers increases as the angle of the curved surface decreases, whereas the thickness increases further owing to the converging downward flows in the 3-D facility. Thus, the Nu_{dn} s in the 3-D system were lower than those in the 2-D system.

The correlation of the angular Nu_{dn} ratio for MassTER-OP2 was developed as follows:

$$Nu_{2D} = 0.228 + (1.32 \times 10^{-2})\theta + (4.02 \times 10^{-4})\theta^2 - (1.56 \times 10^{-6})\theta^3 - (2.19 \times 10^{-6})\theta^4 + (2.31 \times 10^{-9})\theta^5. \quad (17)$$

As the MassTER-OP2 results were similar regardless of variations in Ra'_H , the developed correlation was not influenced by Ra'_H . The developed correlation (line) and experimental results (symbols) for MassTER-OP2 are shown in Fig. 8.

A multiplier to extrapolate the MassTER-OP2 results into 3-D was derived. The multiplier includes an Ra'_H factor to indicate variation of the MassTER-OP3 results with Ra'_H . The developed multiplier was expressed by:

$$\phi = 0.7e^{0.00001(\theta-57.95)^3 \left(\frac{1.81 \times 10^{13}}{Ra'_H}\right)^{0.24}} + 0.122. \quad (18)$$

Consequently, the correlation of MassTER-OP3 could be described by multiplication of the MassTER-OP2 correlation and the multiplier:

$$Nu_{3D} = Nu_{2D} \times \phi = Nu_{2D} \left(0.7e^{0.00001(\theta-57.95)^3 \left(\frac{1.81 \times 10^{13}}{Ra'_H}\right)^{0.24}} + 0.122 \right). \quad (19)$$

Fig. 9 indicates the developed correlations (lines) and experimental results (symbols) for MassTER-OP3 with three different Ra'_H values. It was possible to infer the 3-D results from the 2-D results

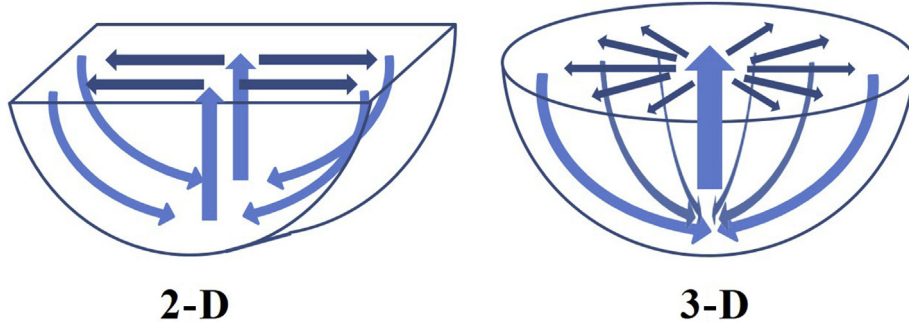


Fig. 7. Difference of flow pattern between two-dimensional (2-D) and 3-D geometries.

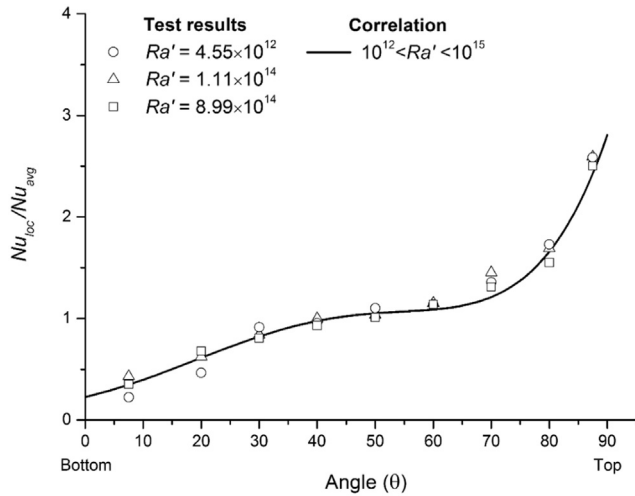


Fig. 8. Heat transfer correlation for MassTER-OP2.

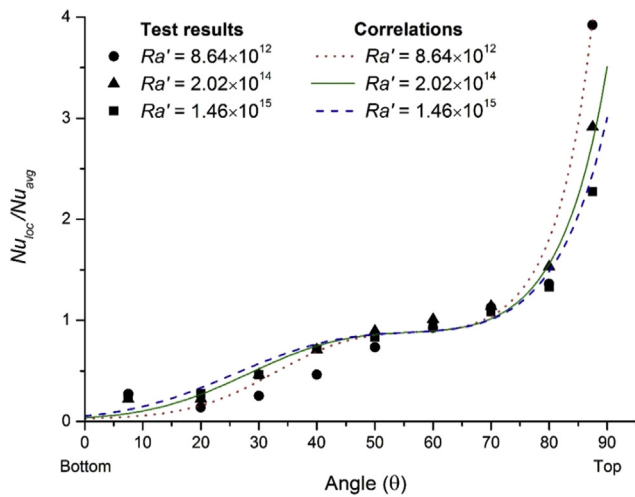
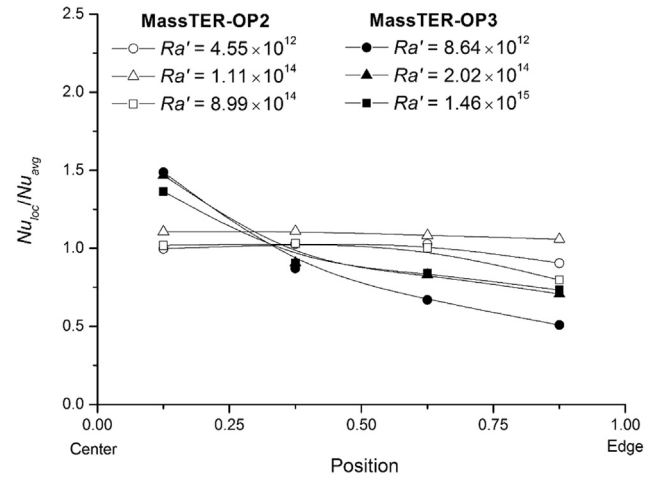


Fig. 9. Heat transfer correlation for MassTER-OP3.

Fig. 10. Comparison of local Nu_{dn} for the top plate between MassTER-OP2 and MassTER-OP3.

5. Conclusions

We investigated IVR phenomena using 2-D and 3-D facilities (MassTER-OP2 and MassTER-OP3) for three different heights: 0.042 m, 0.1 m, and 0.167 m. As was done in the other studies listed in Table 1, this work was performed with idealized simplified configurations and assuming a homogeneous oxide pool. Based on an analogy between heat and mass transfer, mass transfer experiments were performed using a $\text{CuSO}_4\text{--H}_2\text{SO}_4$ electroplating system.

By performing the mass transfer experiments, it was possible to achieve a high Ra'_H ranging from 10^{12} to 10^{15} with small facilities; uniform heat generation and isothermal cooling were maintained. An inverted arrangement of the test facilities was devised to simulate the downward buoyancy along the curved surface; a cathode was used for measurement. The Schmidt number was 2,014 in all cases.

The measured mean Nus of the curved surface (Nu_{dn}) were 37% lower, and those of the top plate (Nu_{up}) were 47% greater than those of other existing studies, owing to the high Pr used in this study. The influence of Pr on Nu_{dn} and Nu_{up} was discussed.

For both MassTER-OP2 and MassTER-OP3, the local Nu_{dn} s of the curved surface increased with its angle. In the lower section, owing to thickening of the thermal boundary layer, the local Nu_{dn} s of the 2-D tests were higher than those in the 3-D tests. In the upper section, Ra'_H had an influence on the 3-D results, but not on the 2-D results. A correlation was developed for MassTER-OP2; we suggested a multiplier that allowed conversion of results from 2-D to 3-D. The local Nu_{up} s for the MassTER-OP3 on the top plate decreased steadily, whereas those for the MassTER-OP2 were almost consistent, slightly decreasing near the edge. This is also caused by the differing flows in the 2-D and 3-D geometries. Using the proper definition of the volumetric heat flux expression in Ra'_H for 2-D, consistent test results for 2-D and 3-D were obtained.

The originality of this study lies in the adoption of a mass transfer system to achieve high buoyancy, the comparison of 2-D and 3-D results, the specified definition of the 2-D modified Rayleigh number, and the multiplier that enables extrapolation of 2-D results to 3-D ones. For IVR phenomena, for which not many experiments have been performed, this study contributes to the accumulation of the experimental database, especially for higher values of Ra'_H . As further study, we are planning to simulate other transient phenomena such as crust formation and debris formation in the oxide pool.

by expressing the 3-D correlation as a multiplication of the 2-D correlation and multiplier.

As the angular variations of heat flux are caused by the development of downward flow along the curved surface, as shown in Fig. 1, no influence of Pr , which governs the relative thicknesses of the thermal and momentum boundary layers, appeared. Hence, we suggest that the Pr of the working fluid does not affect the Nu_{dn} ratios of the curved surface.

4.4.2. Top plate

Fig. 10 shows the measured local Nu_{up} with regard to the position of the top plate for the MassTER-OP2 (open symbols) and MassTER-OP3 (solid symbols) systems. Although there is some scattering in the measured results, the MassTER-OP3 results decreased consistently from the center to the edge. However, the MassTER-OP2 results showed a uniform distribution. On the top plate, the 3-D flows disperse radially and are expected to be weakened as they proceed to the edges. However, the 2-D flows move linearly and are not expected to be significantly weakened, as discussed previously.

Conflicts of interest

There is no conflict of interest with any financial organization regarding the material discussed in the manuscript.

Acknowledgments

This study was sponsored by the Ministry of Science and ICT (MSIT), Korea and was supported by the Nuclear Research & Development program grant funded by the National Research Foundation (NRF) (grant code: 2017M2A8A4015283).

References

- [1] J.M. Bonnet, J.M. Seiler, Thermal hydraulic phenomena in corium pools: the BALI experiment, in: 7th International Conference on Nuclear Engineering, Tokyo, Japan, 1999.
- [2] J.K. Lee, K.Y. Shu, K.J. Lee, J.I. Yun, Experimental study of natural convection heat transfer in a volumetrically heated semicircular pool, *Ann. Nucl. Energy* 73 (2014) 432–440.
- [3] O. Kymäläinen, H. Tuomisto, O. Hongisto, T.G. Theofanous, Heat flux distribution from a volumetrically heated pool with high Rayleigh number, *Nucl. Eng. Des.* 149 (1994) 401–408.
- [4] M. Helle, O. Kymäläinen, H. Tuomisto, Experimental Data on Heat Flux Distribution from a Volumetrically Heated Pool with Frozen Boundaries, IVO Power Engineering Ltd, 1998.
- [5] B.R. Sehgal, V.A. Bui, T.N. Dinh, J.A. Green, G. Kolb, SIMECO experiments on in-vessel melt pool formation and heat transfer with and without a metallic layer, in: Proceedings of In-vessel Core Debris Retention and Coolability Workshop, Garching, Germany, 1998.
- [6] F.J. Asfia, V.K. Dhir, An experimental study of natural convection in a volumetrically heated spherical pool bounded on top with a rigid wall, *Nucl. Eng. Des.* 163 (1996) 333–348.
- [7] T.G. Theofanous, M. Maguire, S. Angelini, T. Salmassi, The first results from the ACOPO experiment, *Nucl. Eng. Des.* 169 (1997) 49–57.
- [8] F.P. Incropera, D.P. Dewitt, Fundamentals of Heat and Mass Transfer, fifth ed., John Wiley & Sons Inc., New York, 2003, pp. 614–619.
- [9] A. Bejan, Convection Heat Transfer, second ed., John Wiley & Sons Inc., New York, 1995, pp. 466–514.
- [10] V.G. Levich, Physicochemical Hydrodynamics, second ed., Prentice-Hall, New Jersey, 1962.
- [11] J.N. Agar, Diffusion and convection at electrodes, *Discuss. Faraday Soc.* 1 (1947) 27–37.
- [12] J.R. Selman, C.W. Tobias, Mass transfer measurement by the limiting current technique, *Adv. Chem. Eng.* 10 (1978) 211–318.
- [13] M.M. Zaki, I. Nirdosh, G.H. Sedahmed, Forced convection mass transfer inside large hemispherical cavities under laminar flow conditions, *Chem. Eng. Commun.* 159 (1997) 161–171.
- [14] B.J. Chung, J.H. Eoh, J.H. Heo, Visualization of natural convection on a horizontal cylinder, *Heat Mass Transf.* 47 (2011) 1445–1452.
- [15] S.H. Ko, D.W. Moon, B.J. Chung, Applications of electroplating method for heat transfer studies using analogy concept, *Nucl. Eng. Technol.* 38 (2006) 251–258.
- [16] B.J. Ko, M.H. Kim, B.J. Chung, An experimental study on the transition criteria of open channel natural convection flows, *J. Mech. Sci. Technol.* 26 (2012) 1227–1234.
- [17] J.Y. Moon, B.J. Chung, Time-dependent Rayleigh–Benard convection: cell formation and Nusselt number, *Nucl. Eng. Des.* 274 (2014) 146–153.
- [18] M.S. Chae, B.J. Chung, Natural convection heat transfer in a uniformly heated horizontal pipe, *Heat Mass Transf.* 50 (2014) 115–123.
- [19] H.K. Park, B.J. Chung, Mass transfer experiments for the heat load during in-vessel retention of core melt, *Nucl. Eng. Technol.* 48 (2016) 906–914.
- [20] G.U. Kang, B.J. Chung, Natural convection heat transfer characteristics in vertical cavities with active and inactive top and bottom disks, *Int. J. Heat Mass Transfer* 87 (2015) 390–398.
- [21] S.H. Hong, B.J. Chung, Variations of the optimal fin spacing according to Prandtl number in natural convection, *Int. J. Therm. Sci.* 101 (2016) 1–8.
- [22] E.J. Fenech, C.W. Tobias, Mass transfer by free convection at horizontal electrodes, *Electrochim. Acta* 2 (1960) 311–325.
- [23] C.K. Lim, B.J. Chung, Influence of a center anode in analogy experiments of long flow ducts, *Int. Commun. Heat Mass Transfer* 56 (2014) 174–180.
- [24] T.N. Dinh, R.R. Nourgaliev, B.R. Sehgal, On heat transfer characteristics of real and simulant melt pool experiments, *Nucl. Eng. Des.* 169 (1997) 151–164.
- [25] H.K. Park, B.J. Chung, Optimal tip clearance in the laminar forced convection heat transfer of a finned plate in a square duct, *Int. Commun. Heat Mass* 63 (2016) 73–81.
- [26] S.K. Kim, B.J. Chung, Heat load imposed on reactor vessels during in-vessel retention of core melts, *Nucl. Eng. Des.* 308 (2016) 1–8.
- [27] Y. Konishi, Y. Nakamura, Y. Fukunaka, K. Tsukada, K. Hanasaki, Anodic dissolution phenomena accompanying supersaturation of copper sulfate along a vertical plane copper anode, *Electrochim. Acta* 48 (2003) 2615–2624.
- [28] W.G. Steele, H.W. Coleman, Experimental and Uncertainty Analysis for Engineers, second ed., John Wiley & Son, Canada, 1999.